Supplementary Information

Quantum Well–Inspired Energy Level Design in Multicomponent Organic Solar Cells for Improved Energy Loss Management

Dr. Top Archie Dela Peña,[#] Dr. Issatay Nadinov,[#] Dr. Tzu-Yen Huang, Dr. Zengshan Xing, Dr. Lu Chen, Dr. Yao Li, Dr. Sheena Anne Garcia, Junyin Dong, Yongmin Luo, Prof. King Lun Yeung, Prof. Jafar I. Khan, Prof. Guangye Zhang, Prof. Jiaying Wu, Prof. Tze Chien Sum, Prof. Ruijie Ma, Prof. Omar F. Mohammed, Prof. Yeng Ming Lam*

Supplementary Figures

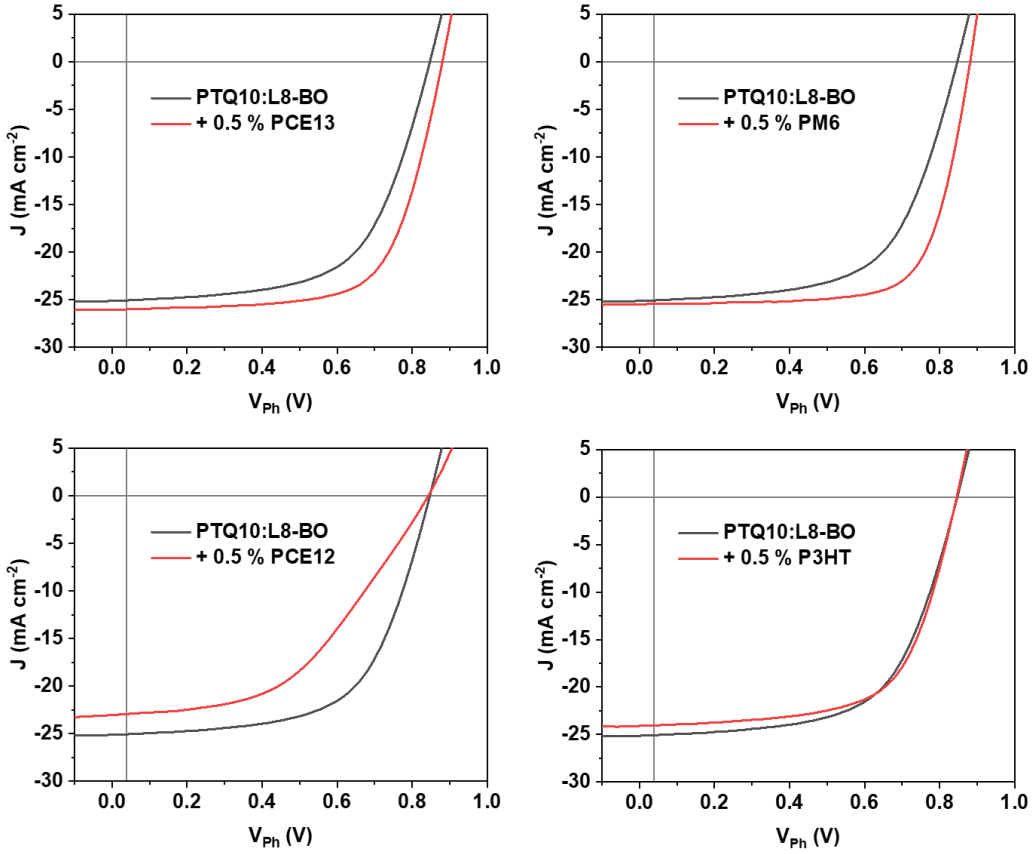

Fig. S1. J-V curves of PTQ10:L8-BO devices modified with 0.5 % guest donor.

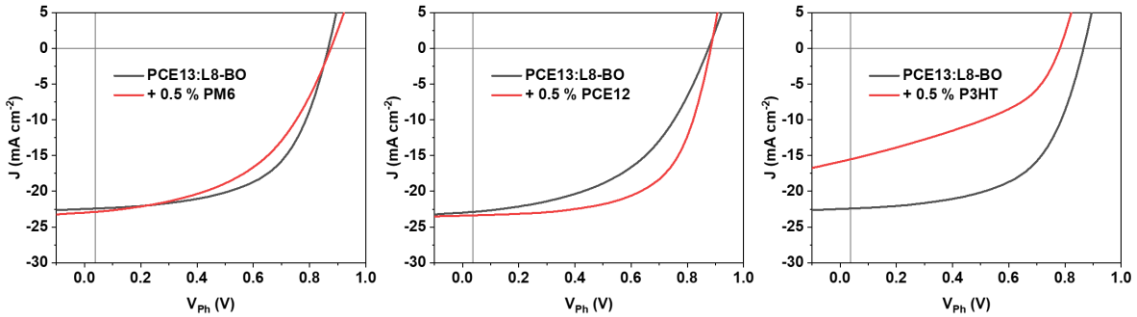

Fig. S2. J-V curves of PCE13:L8-BO devices modified with 0.5 % guest donor.

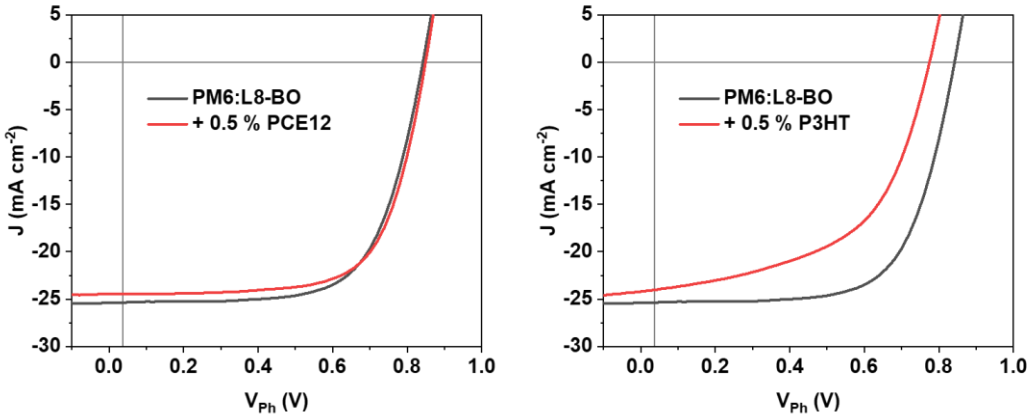

Fig. S3. J-V curves of PM6:L8-BO devices modified with 0.5 % guest donor.

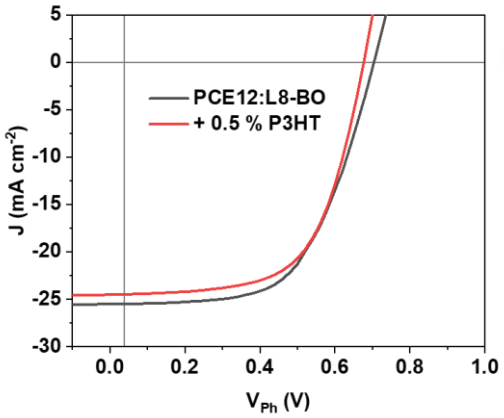

Fig. S4. J-V curves of PCE12:L8-BO devices modified with 0.5 % guest donor.

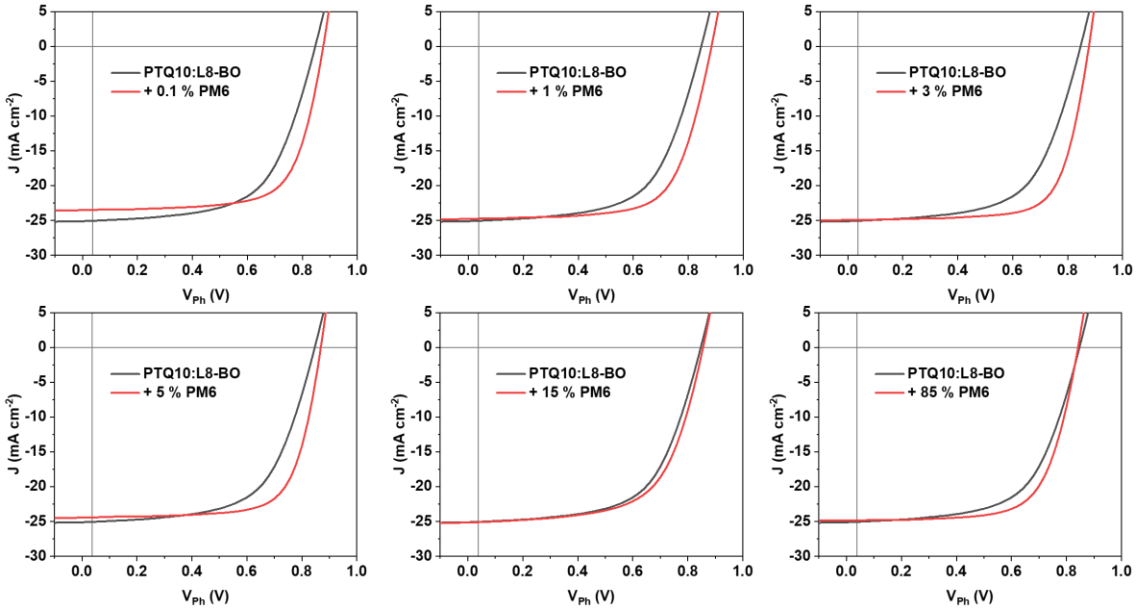

Fig. S5. J-V curves of PTQ10:L8-BO devices with varying PM6 composition.

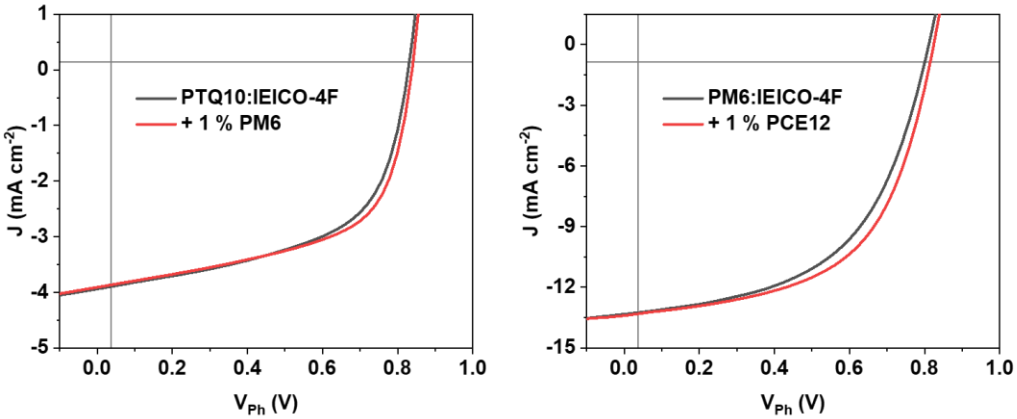

Fig. S6. J-V curves of polymer:IEICO-4F devices with 1 % guest donor.

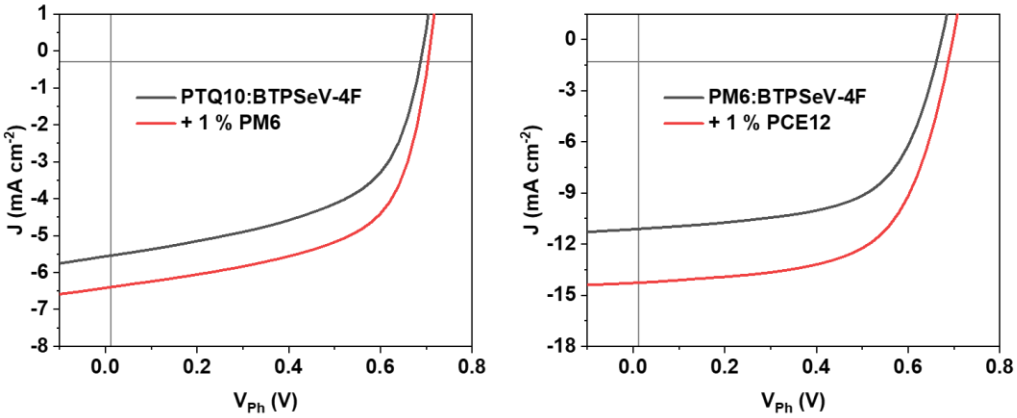

Fig. S7. J-V curves of polymer:BTPSeV-4F devices with 1 % guest donor.

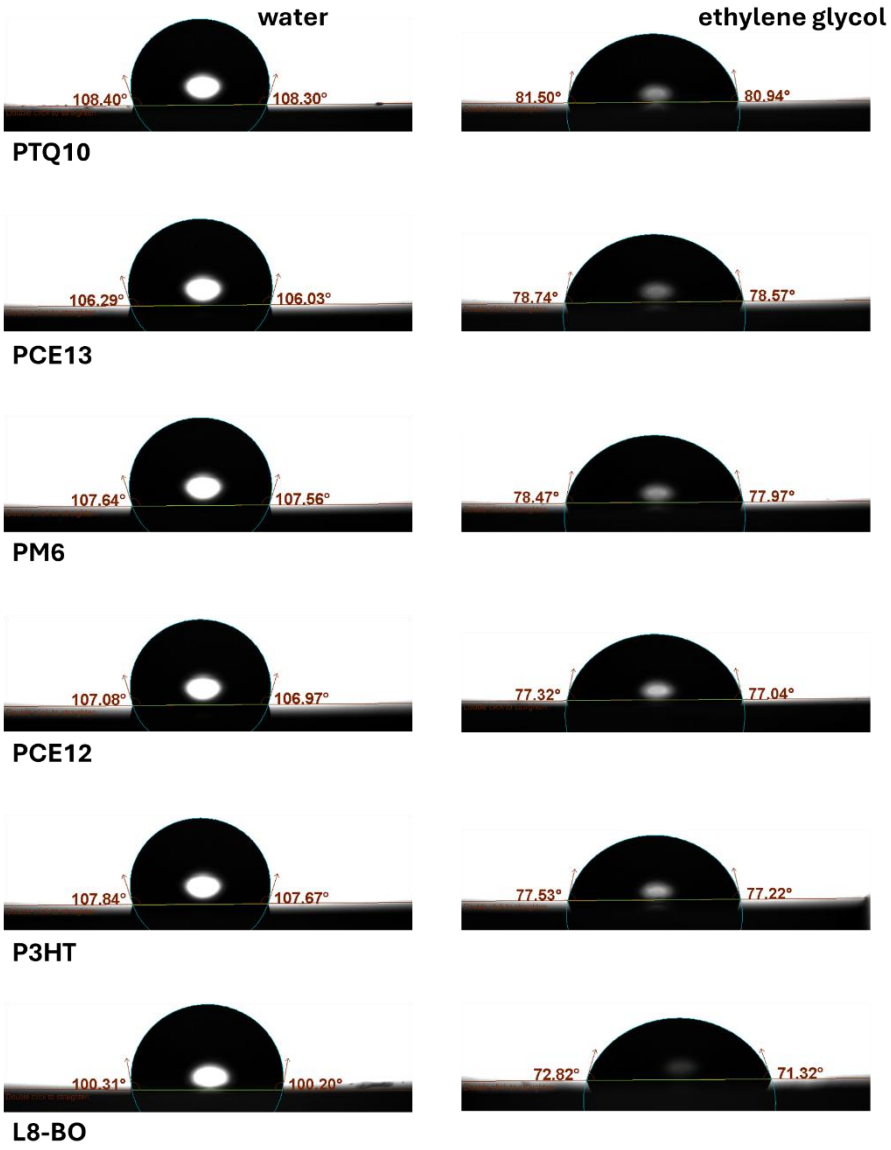

Fig. S8. Contact angle measurement of neat donor (or acceptor) films on glass substrates.

Short discussion:

The surface free energies (SFEs) were calculated using the Owens, Wendt, Rabel, and Kaelble (OWRK) method, with deionized water and ethylene glycol as the liquid droplet medium. The results are shown in **Table S8**.

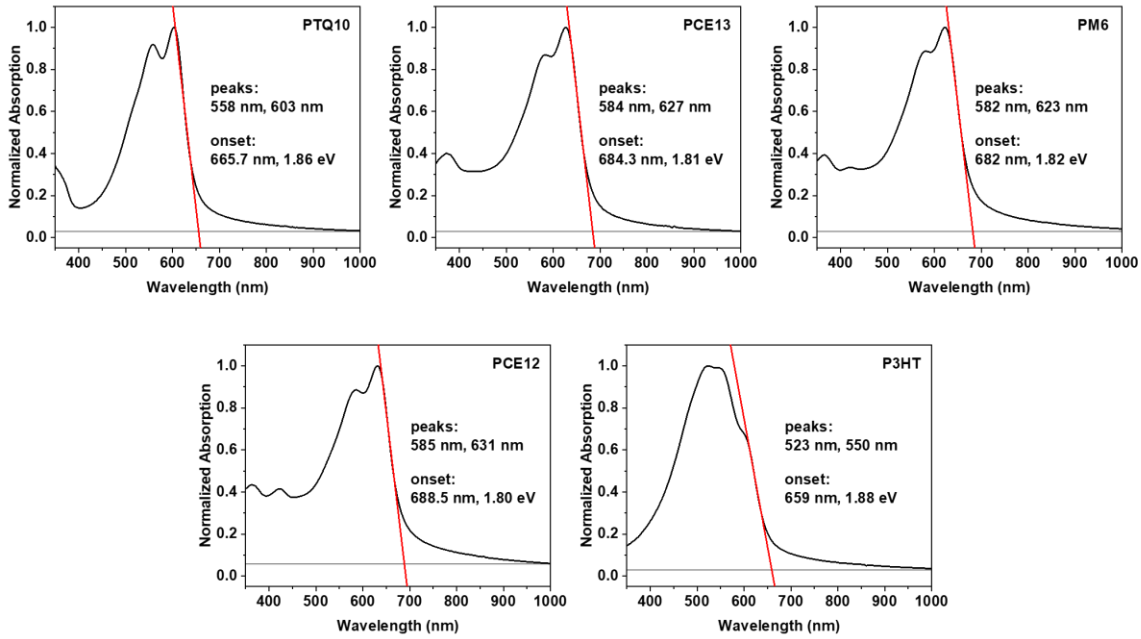

Fig. S9. Optical absorption spectra of neat donor films on quartz substrates. The peak positions and absorption onset are indicated. In this work, absorption onset is used as the reference bandgap for energy loss calculations, consistent with the SQ limit approximations.

Short discussion:

PTQ10 has a hypsochromic (blue-shifted) optical absorption compared to PM6. This makes the PTQ10 and PM6 a perfect representative primary and secondary donor combination, allowing the more direct exploration of the PQCE and relevant charge transfer processes through both steady-state and transient optical methods.

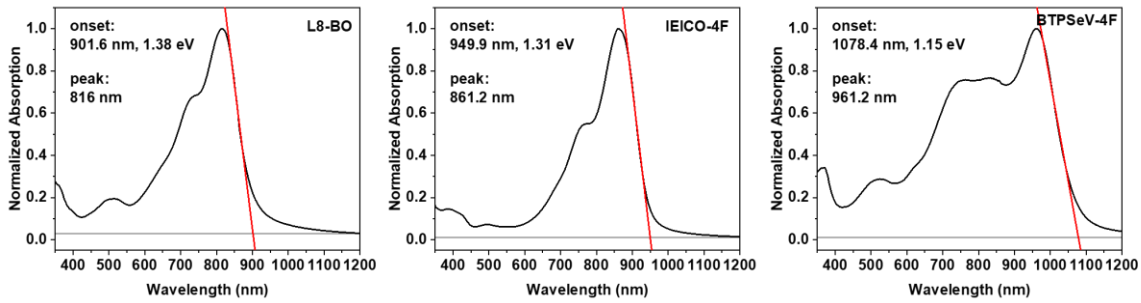

Fig. S10. Optical absorption spectra of neat acceptor films on quartz substrates. The peak positions and absorption onset are indicated. In this work, absorption onset is used as the reference bandgap for energy loss calculations, consistent with the SQ limit approximations.

Short discussion:

L8-BO is the commonly used small-molecule acceptor for most high-performance OSCs reported recently. The bandgap of L8-BO (1.38 eV, estimated through absorption onset) is considered a low-bandgap acceptor and is nearly ideal for most single-junction solar cells. Meanwhile, the more NIR bandgap IEICO-4F and BTPSeV-4F could be more beneficial for multijunction solar cell applications. Nevertheless, L8-BO, IEICO-4F, and BTPSeV-4F are all among the highly promising acceptor molecules developed recently.

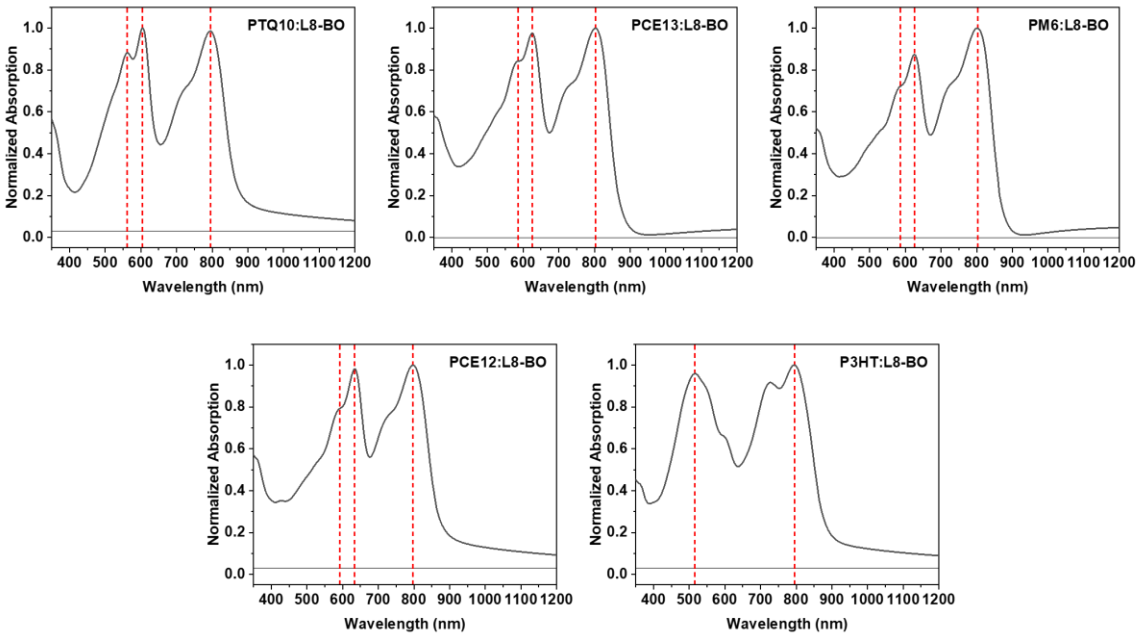

Fig. S11. Optical absorption spectra of donor:acceptor blend films on quartz substrates. The peak positions are indicated with dashed lines.

Short discussion:

Similar to neat donor films, the PTQ10 shows hypsochromic (blue-shifted) optical absorption compared to PM6 when blended with L8-BO. These spectral differences will make the transient optical characterizations more intuitive to interpret for PQCE than the other donor combinations.

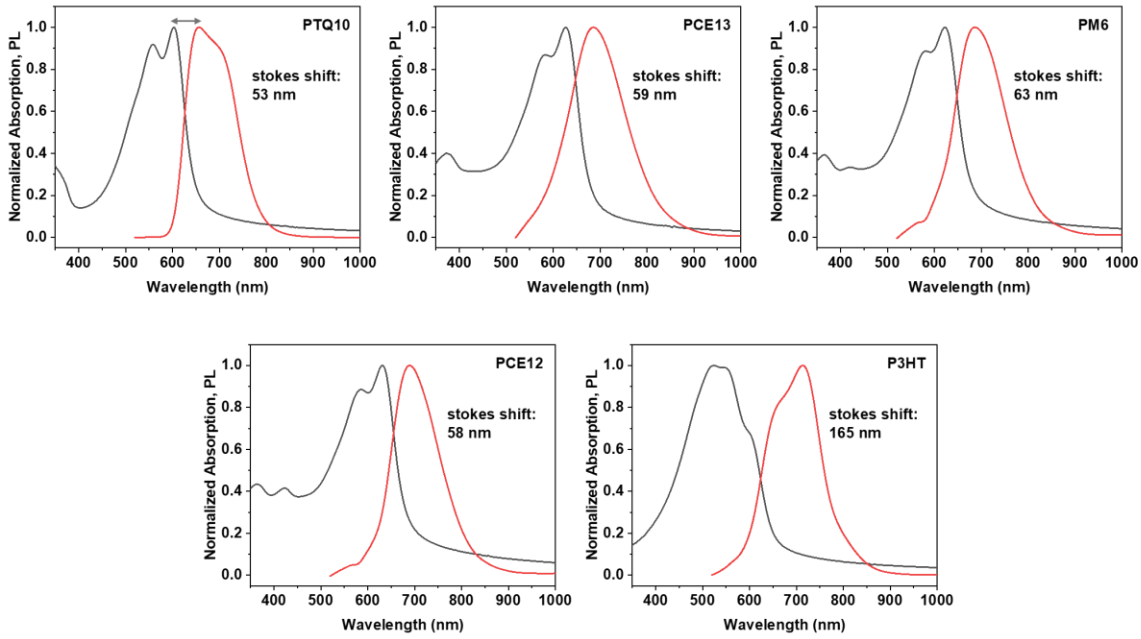

Fig. S12. Optical absorption and emission spectra of neat donor films on quartz substrates. The photoluminescence was obtained through a 514 nm laser as the excitation source. The indicated Stokes shifts are estimated from the peak 0-0 transition band peaks.

Short discussion:

The Stokes shift is caused by the vibrational relaxation and nuclear reconfiguration to achieve the most stable (i.e., lowest energy) configuration in response to optical excitation of charge carriers from the ground state into the excited state. Such nuclear reconfiguration happens within the time frame much earlier than optical emissions (i.e., photoluminescence). Hence, the Stokes shift calculated from the 0-0 transition band peaks of the absorption and emission spectra relates to the degree of nuclear reconfiguration. In particular, smaller Stokes shifts are known characteristics of more crystalline materials or ordered molecular assemblies [1]. In later discussions and **Fig. S13**, the Stokes shift from PTQ10 with 1 % PM6 is shown to be equivalent to pure PTQ10. This indicates that 1 % PM6 does not influence the overall molecular packing of PTQ10, eliminating the possibility of molecular-level mixing. The case is, however, different for PM6 with 1 % PCE12, where molecular-level mixing is expected due to their miscibility (**Fig. 3a** and **Table S8**).

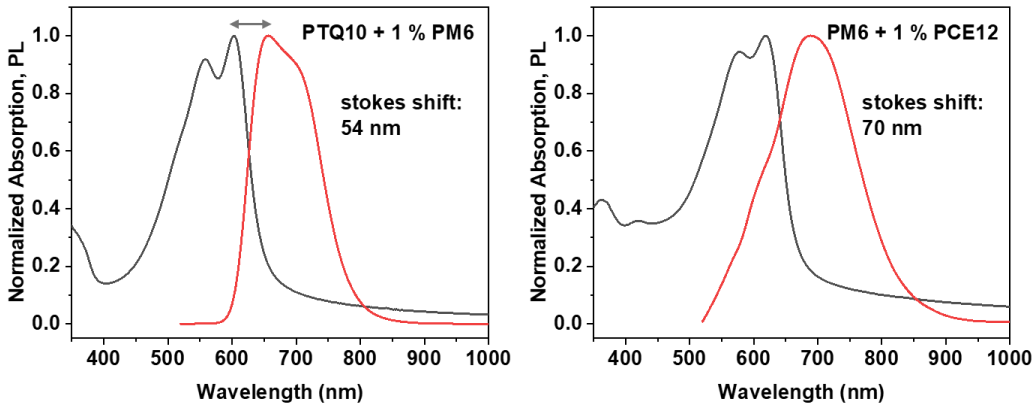

Fig. S13. Optical absorption and emission spectra of donor blend films on quartz substrates. The photoluminescence was obtained through a 514 nm laser as the excitation source. The indicated Stokes shifts are estimated from the peak 0-0 transition band peaks.

Short discussion:

The Stokes shift for PTQ10 with 1 % PM6 (54 nm) is comparable with pure PTQ10 (53 nm). This indicates that the addition of 1 % PM6 does not alter the overall molecular packing of PTQ10, eliminating the possibility of molecular-level mixing. This can also be inferred from the interaction parameter derived from contact angles (**Fig. 3a** and **Table S8**), such that PM6 does not have sufficient interaction strength to undergo molecular-level mixing with PTQ10. Generally, an interaction parameter of nearly zero is necessary for molecular-level mixing [2]. On the other hand, PM6 is still highly attracted to PTQ10 while it tends to phase separate with L8-BO, thereby prompting PTQ10 molecules to likely engulf these PM6 molecules.

However, the Stokes shift for PM6 with 1 % PCE12 (70 nm) is quite higher than pure PM6 (63 nm). This indicates that PCE12 does significantly alter the overall molecular packing of PM6. From the interaction parameters (**Fig. 3a** and **Table S8**), PM6 and PCE12 are miscible. Based on rough estimations from optical absorption spectra (**Fig. 3b**), around 15 - 20 % of PM6 assemblies have been alloyed with PCE12. Hence, these alloyed phases are likely to extend up to the junction with charge-transporting layers, forming a parallel-like morphology with PM6-rich domains and minimizing the impacts of PQCE.

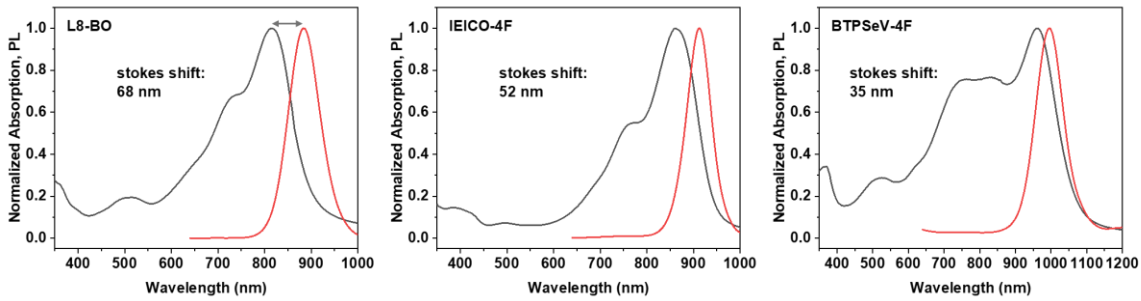

Fig. S14. Optical absorption and emission spectra of neat acceptor films on quartz substrates. The photoluminescence was obtained through a 633 nm laser as the excitation source. The indicated Stokes shifts are estimated from the peak 0-0 transition band peaks.

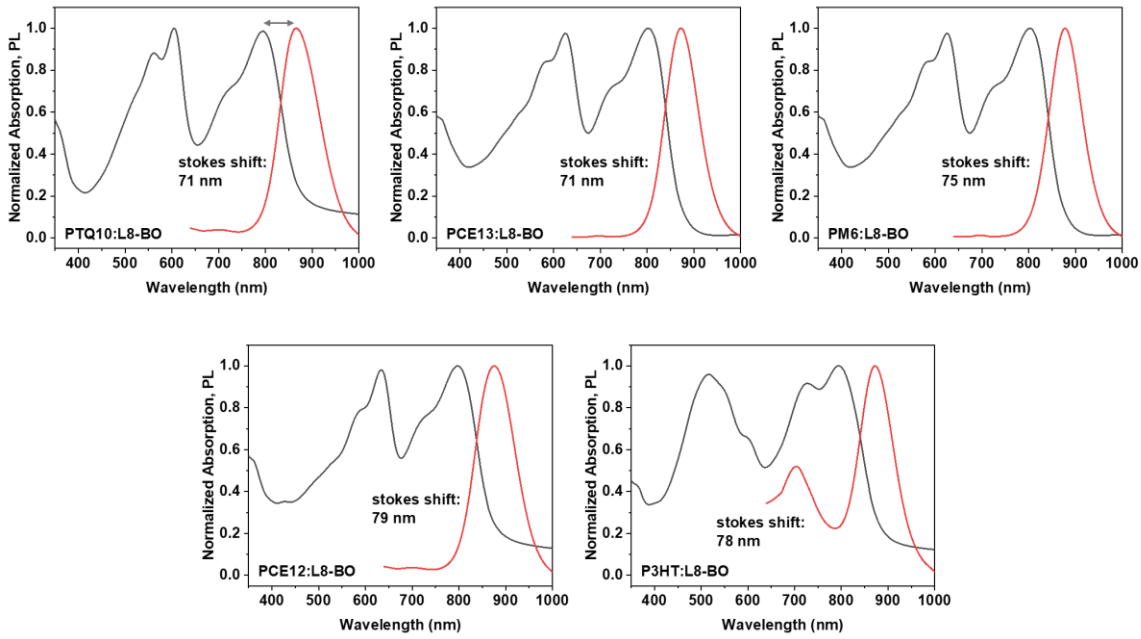

Fig. S15. Optical absorption and emission spectra of donor:acceptor blend films on quartz substrates. The photoluminescence was obtained through a 633 nm laser as the excitation source. The indicated Stokes shifts are estimated from the peak 0-0 transition band peaks.

Short discussion:

As with most of the emission spectra (red curve) in high-efficiency organic donor:acceptor blends reported in the literature, only the acceptor emission features are clearly visible while the donor emissions are negligible. For low singlet exciton dissociation efficiency systems such as P3HT:L8-BO, the donor emission can be visible, but the acceptor emission remains dominant. These suggest that the primary mechanism for free carrier losses is the back transfer of hole polarons from the donor molecule to the acceptor molecule (as illustrated below). Accordingly, this work focuses on manipulating these hole polarons through PQCE.

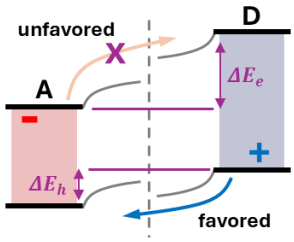

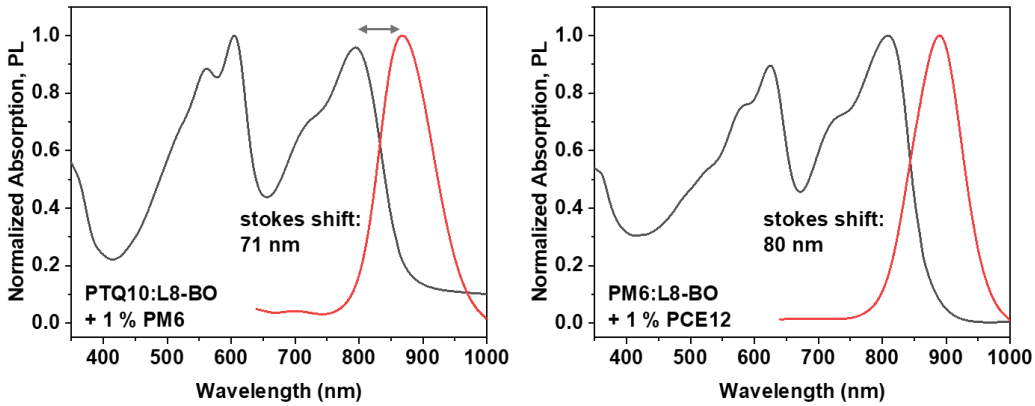

Fig. S16. Optical absorption and emission spectra of donor:acceptor with 1 % guest donor blend films on quartz substrates. The photoluminescence was obtained through a 633 nm laser as the excitation source. The indicated Stokes shifts are estimated from the peak 0-0 transition band peaks.

Short discussion:

Similar to the donor blends of PTQ10 and PM6 **(Fig. S12-S13)**, the addition of 1 % PM6 in the PTQ10:L8-BO does not cause sizable changes in the Stokes shift. This indicates that PM6 does not alter the overall molecular packing of both PTQ10 and L8-BO in the bulk. Meanwhile, the addition of 1 % PCE12 in the PM6:L8-BO does sizably change the Stokes shift. The same effect was consistent with the previous discussion from the donor blends of PM6 and PCE12 **(Fig. S12-S13)**.

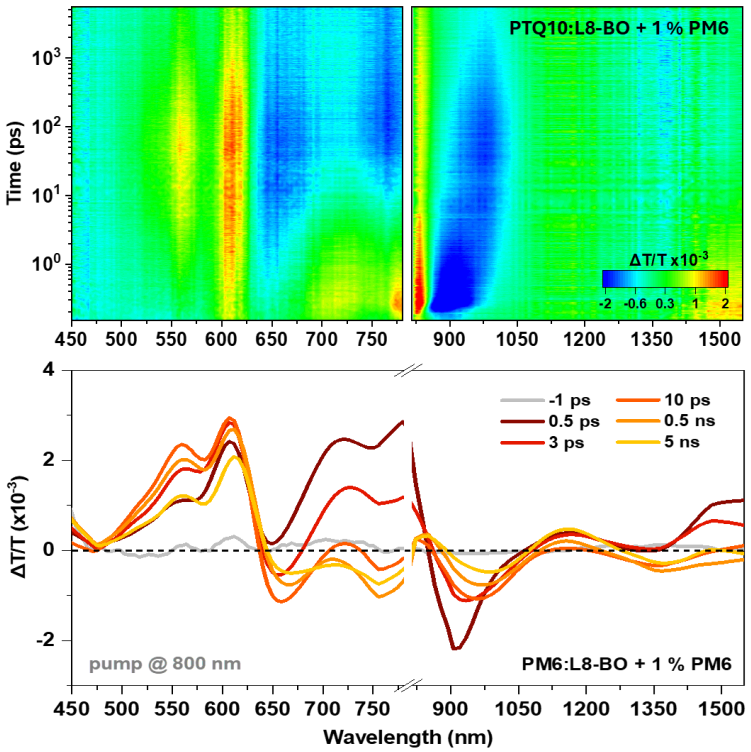

Fig. S17. Pseudo 2D plot and spectral line cuts for PTQ10:L8-BO with 1 % PM6. These data were obtained using transient absorption spectroscopy (TAS) with an 800 nm pump laser, for selective L8-BO excitation, at a fluence of 3 μJ/cm².

Short discussion:

Immediately after selective excitation of the acceptor L8-BO using an 800 nm pump laser, the polarons (i.e., free charge carriers) photo-bleaching (PB) are already visible, indicating that some L8-BO singlet excitons undergo an ultrafast dissociation and free carrier generation. The same phenomenon is consistent with several reports of efficient organic solar cells [3, 4], and the other donor:acceptor blends explored in this work.

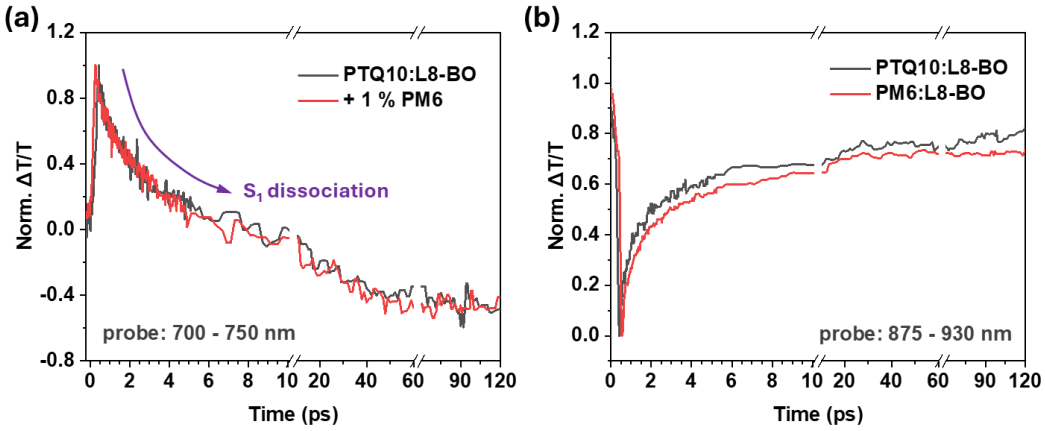

Fig. S18. Singlet exciton dissociation kinetics for PTQ10 and PM6-based blends. **(a)** Comparison of PTQ10:L8-BO control and with the addition of 1 % PM6. **(b)** Comparison of PTQ10:L8-BO and PM6:L8-BO. These data were obtained using transient absorption spectroscopy with an 800 nm pump laser at a fluence of 3 μJ/cm².

Short discussion:

Upon selective L8-BO excitation with an 800 nm pump laser, the L8-BO singlet exciton dissociation appears independent of the addition of 1 % PM6. Hence, PTQ10:L8-BO and PTQ10:L8-BO + 1 % PM6 display an equivalent S_1 dissociation dynamics based on L8-BO ground state bleach (GSB) **(Fig. S18a)**, also shown in the L8-BO S_1 photo-induced absorption (PIA) in **Fig. 4d** of the main text. Meanwhile, the L8-BO singlet exciton dissociation in PTQ10:L8-BO is quite faster than PM6:L8-BO from the L8-BO S_1 PIA **(Fig. S18b)**, indicating that L8-BO dissociation with PTQ10 and PM6 heterointerfaces is not of equivalent rates.

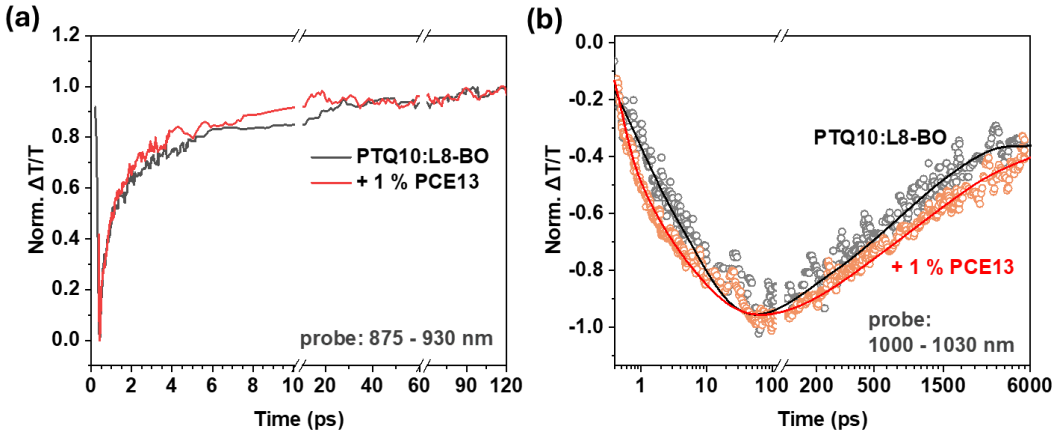

Fig. S19. Charge carrier dynamics for PTQ10:L8-BO with 1 % PCE13. **(a)** Comparison of singlet exciton dissociation kinetics for PTQ10:L8-BO control and with the addition of 1 % PCE13. **(b)** Comparison of polaron generation and recombination kinetics for PTQ10:L8-BO control and with the addition of 1 % PCE13. These data were obtained using transient absorption spectroscopy with an 800 nm pump laser at a fluence of 3 μJ/cm².

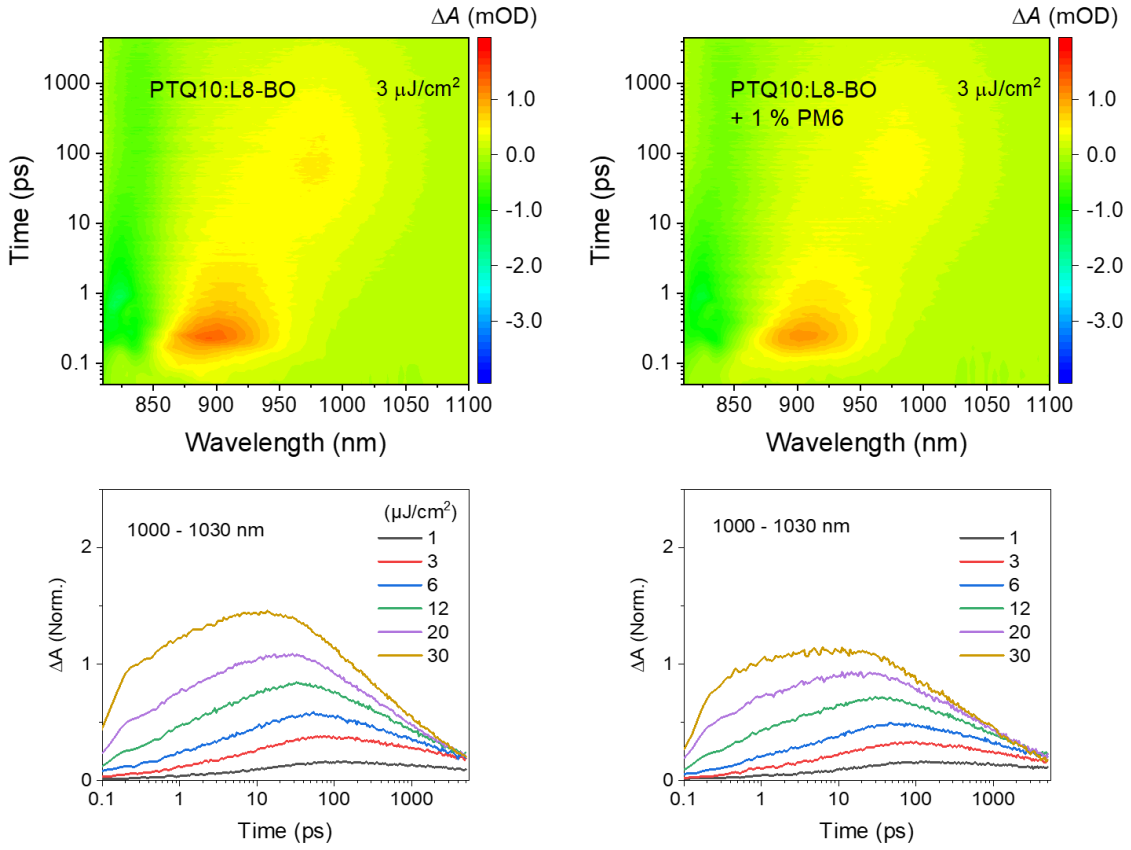

Fig. S20. Fluence-dependent recombination of polarons. These data were obtained using transient absorption spectroscopy with an 800 nm pump laser at a fluence of 3 μJ/cm².

Short discussion:

The polaron recombination at the PTQ10:L8-BO system, regardless of having PM6 as the secondary donor, demonstrates strong excitation laser fluence dependence. This confirms that these polarons dominantly recombine through the bimolecular mechanism.

Supplementary Tables

Table S1. Photovoltaic parameters of PTQ10:L8-BO + 0.5 % guest donor.

Blend	V_{OC} (V)	J_{SC} (mA cm^{-2})	FF	PCE (%)
PTQ10:L8-BO	0.85 ± 0.001	25.5 ± 0.3	0.66 ± 0.02	14.2 ± 0.5
+ 0.5 % PCE13	0.88 ± 0.007	26.6 ± 0.6	0.69 ± 0.01	15.6 ± 0.4
+ 0.5 % PM6	0.88 ± 0.003	25.5 ± 0.1	0.72 ± 0.01	16.2 ± 0.2
+ 0.5 % PCE12	0.84 ± 0.007	23 ± 0.3	0.47 ± 0.01	9.2 ± 0.3
+ 0.5 % P3HT	0.82 ± 0.002	24.4 ± 0.1	0.63 ± 0.01	12.5 ± 0.1

Notes:

1) The statistics were obtained from 10-20 working devices.
2) The precursor solutions are made from a 1:1.2 host donor/acceptor ratio in 15.4 mg/mL, dissolved in chloroform with 0.25 % v/v 1,8-DIO as solvent additive.
3) The percentage of guest donors is based on the weight of the host donor.
4) Guest donors are pre-dissolved in dilute solutions with chloroform and 0.25 % v/v 1,8-DIO.
5) The charge extraction layers, PEDOT:PSS and PFN-Br, are kept constant among all the devices.

Table S2. Photovoltaic parameters of PCE13:L8-BO + 0.5 % guest donor.

Blend	V_{OC} (V)	J_{SC} (mA cm^{-2})	FF	PCE (%)
PCE13:L8-BO	0.87 ± 0.002	22.6 ± 0.1	0.65 ± 0.02	12.7 ± 0.5
+ 0.5 % PM6	0.88 ± 0.001	23.1 ± 0.2	0.50 ± 0.01	10.1 ± 0.2
+ 0.5 % PCE12	0.89 ± 0.003	23.7 ± 0.2	0.64 ± 0.01	13.0 ± 0.2
+ 0.5 % P3HT	0.79 ± 0.003	16.1 ± 0.1	0.42 ± 0.01	5.18 ± 0.1

Notes:

1) The statistics were obtained from 10-20 working devices.
2) The precursor solutions are made from a 1:1.2 host donor/acceptor ratio in 15.4 mg/mL, dissolved in chloroform with 0.25 % v/v 1,8-DIO as solvent additive.
3) The percentage of guest donors is based on the weight of the host donor.
4) Guest donors are pre-dissolved in dilute solutions with chloroform and 0.25 % v/v 1,8-DIO.
5) The charge extraction layers, PEDOT:PSS and PFN-Br, are kept constant among all the devices.

Table S3. Photovoltaic parameters of PM6:L8-BO + 0.5 % guest donor.

Blend	V_{OC} (V)	J_{SC} (mA cm^{-2})	FF	PCE (%)
PM6:L8-BO	0.84 ± 0.001	25.6 ± 0.2	0.68 ± 0.01	14.5 ± 0.1
+ 0.5 % PCE12	0.85 ± 0.002	24.7 ± 0.1	0.69 ± 0.01	14.4 ± 0.2
+ 0.5 % P3HT	0.78 ± 0.003	24.4 ± 0.1	0.55 ± 0.01	10.2 ± 0.1

Notes:

1) The statistics were obtained from 10-20 working devices.
2) The precursor solutions are made from a 1:1.2 host donor/acceptor ratio in 15.4 mg/mL, dissolved in chloroform with 0.25 % v/v 1,8-DIO as solvent additive.
3) The percentage of guest donors is based on the weight of the host donor.
4) Guest donors are pre-dissolved in dilute solutions with chloroform and 0.25 % v/v 1,8-DIO.
5) The charge extraction layers, PEDOT:PSS and PFN-Br, are kept constant among all the devices.

Table S4. Photovoltaic parameters of PCE12:L8-BO + 0.5 % guest donor.

Blend	V_{OC} (V)	J_{SC} (mA cm^{-2})	FF	PCE (%)
PCE12:L8-BO	0.71 ± 0.003	25.6 ± 0.3	0.66 ± 0.02	11.4 ± 0.2
+ 0.5 % P3HT	0.68 ± 0.002	24.8 ± 0.1	0.65 ± 0.01	10.8 ± 0.1

Notes:

1) The statistics were obtained from 10-20 working devices.
2) The precursor solutions are made from a 1:1.2 host donor/acceptor ratio in 15.4 mg/mL, dissolved in chloroform with 0.25 % v/v 1,8-DIO as solvent additive.
3) The percentage of guest donors is based on the weight of the host donor.
4) Guest donors are pre-dissolved in dilute solutions with chloroform and 0.25 % v/v 1,8-DIO.
5) The charge extraction layers, PEDOT:PSS and PFN-Br, are kept constant among all the devices.

Table S5. Photovoltaic parameters of PTQ10:L8-BO with varying % PM6.

% PM6	V_{OC} (V)	J_{SC} (mA cm^{-2})	FF	PCE (%)
0	0.85 ± 0.001	25.5 ± 0.3	0.66 ± 0.02	14.2 ± 0.5
0.1	0.88 ± 0.004	24.3 ± 0.3	0.71 ± 0.01	14.7 ± 0.2
0.5	0.88 ± 0.001	25.5 ± 0.2	0.72 ± 0.01	16.2 ± 0.2
1	0.90 ± 0.003	25.0 ± 0.5	0.73 ± 0.01	15.9 ± 0.5
3	0.89 ± 0.003	24.9 ± 0.3	0.69 ± 0.01	15.1 ± 0.3
5	0.87 ± 0.003	25.1 ± 0.3	0.72 ± 0.01	15.4 ± 0.3
15	0.86 ± 0.002	25.2 ± 0.1	0.64 ± 0.01	13.7 ± 0.1
85	0.84 ± 0.003	25.0 ± 0.1	0.69 ± 0.01	14.5 ± 0.1
100	0.84 ± 0.001	25.6 ± 0.2	0.68 ± 0.01	14.5 ± 0.1

Notes:

1) The statistics were obtained from 10-20 working devices.
2) The precursor solutions are made from a 1:1.2 host donor/acceptor ratio in 15.4 mg/mL, dissolved in chloroform with 0.25 % v/v 1,8-DIO as solvent additive.
3) The percentage of guest donors is based on the weight of the host donor.
4) Guest donors are pre-dissolved in dilute solutions with chloroform and 0.25 % v/v 1,8-DIO.
5) The charge extraction layers, PEDOT:PSS and PFN-Br, are kept constant among all the devices.

Table S6. Photovoltaic parameters of PTQ10:NFA with and without PM6 as guest donor.

NFA	V_{OC} (V)	J_{SC} (mA cm^{-2})	FF	PCE (%)
L8-BO	0.85 ± 0.001	25.5 ± 0.3	0.66 ± 0.02	14.2 ± 0.5
+ 1 % PM6	0.90 ± 0.003	25.0 ± 0.5	0.73 ± 0.01	15.9 ± 0.5
IEICO-4F	0.83 ± 0.001	4.05 ± 0.1	0.58 ± 0.01	1.95 ± 0.1
+ 1 % PM6	0.85 ± 0.002	3.97 ± 0.1	0.58 ± 0.01	1.93 ± 0.1
BTPSeV-4F	0.70 ± 0.001	5.56 ± 0.2	0.58 ± 0.02	2.12 ± 0.2
+ 1 % PM6	0.72 ± 0.002	6.64 ± 0.2	0.60 ± 0.01	2.82 ± 0.2

Notes:

1) The statistics were obtained from 10-20 working devices.
2) The precursor solutions are made from a 1:1.2 host donor/acceptor ratio in 15.4 mg/mL, dissolved in chloroform with 0.25 % v/v 1,8-DIO as solvent additive.
3) The percentage of guest donors is based on the weight of the host donor.
4) Guest donors are pre-dissolved in dilute solutions with chloroform and 0.25 % v/v 1,8-DIO.
5) The charge extraction layers, PEDOT:PSS and PFN-Br, are kept constant among all the devices.

Short discussion:

Due to ineffective IE level alignment with PTQ10, the devices with NIR photoabsorbers, IEICO-4F and BTP-SeV-4F, cannot achieve comparable PCEs to L8-BO. On the other hand, the impacts of PQCE in energy loss minimization remain observable even with these NIR electron-accepting photoabsorbers.

Table S7. Photovoltaic parameters of PM6:NFA with and without PCE12 as guest donor.

NFA	V_{OC} (V)	J_{SC} (mA cm^{-2})	FF	PCE (%)
L8-BO	0.84 ± 0.001	25.6 ± 0.2	0.68 ± 0.01	14.5 ± 0.1
+ 0.5 % PCE12	0.85 ± 0.002	24.7 ± 0.1	0.69 ± 0.01	14.4 ± 0.2
IEICO-4F	0.81 ± 0.001	13.5 ± 0.1	0.54 ± 0.01	5.86 ± 0.1
+ 0.5 % PCE12	0.83 ± 0.002	13.6 ± 0.4	0.58 ± 0.01	6.37 ± 0.4
BTPSeV-4F	0.67 ± 0.001	11.3 ± 0.1	0.62 ± 0.01	4.65 ± 0.1
+ 0.5 % PCE12	0.70 ± 0.002	14.5 ± 0.1	0.64 ± 0.01	6.37 ± 0.1

Notes:

1) The statistics were obtained from 10-20 working devices.
2) The precursor solutions are made from a 1:1.2 host donor/acceptor ratio in 15.4 mg/mL, dissolved in chloroform with 0.25 % v/v 1,8-DIO as solvent additive.
3) The percentage of guest donors is based on the weight of the host donor.
4) Guest donors are pre-dissolved in dilute solutions with chloroform and 0.25 % v/v 1,8-DIO.
5) The charge extraction layers, PEDOT:PSS and PFN-Br, are kept constant among all the devices.

Short discussion:

Due to ineffective IE level alignment with PM6, the devices with NIR photoabsorbers, IEICO-4F and BTP-SeV-4F, cannot achieve comparable PCEs to L8-BO. On the other hand, the impacts of PQCE in energy loss minimization remain observable even with these NIR electron-accepting photoabsorbers.

Table S8. Interaction parameter from surface free energies.

Sample	SFE ($mN\ m^{-1}$)	$\chi_{x,L8\text{-}BO}$	$\chi_{x,PTQ10}$	$\chi_{x,PCE13}$	$\chi_{x,PM6}$	$\chi_{x,PCE12}$
PTQ10	26.34	0.80	/	0.33	0.25	0.26
PCE13	30.60	0.26	0.33	/	1.06	1.03
PM6	23.69	1.42	0.25	1.06	/	0.003
PCE12	23.93	1.34	0.26	1.03	0.003	/
P3HT	21.17	2.52	0.89	2.15	0.22	0.22
L8-BO	32.64	/	0.80	0.26	1.42	1.34

Notes:

1) The surface free energies (SFEs) were estimated using the Owens, Wendt, Rabel, and Kaelble (OWRK) method.
2) The Flory-Huggins interaction parameter (χ) of x to y is estimated using the obtained surface free energies and the equation below:

$$\chi_{x,y} \propto \left(\sqrt{SFE_x} - \sqrt{SFE_y}\right)^2$$

Short discussion:

According to the general formalism, $\chi_{x,y}$ values nearly 0 indicate molecular-level mixing between x and y, known as molecular alloys. Meanwhile, values close (but not approaching) zero indicate a strong attraction between x and y without forming molecular alloys. Lastly, as the values become larger, the x and y molecular interactions weaken, suggestive of stronger phase segregation.

Table S9. Lamellar Stacking in the in-plane (IP) direction from GIWAXS.

Materials	Peak location [Å^{-1}]	Stacking distance [Å]	FWHM of Peak [Å^{-1}]	CCL [Å]
PTQ10	0.255	24.594	0.091	62.189
PM6	0.281	22.331	0.093	60.982
PCE12	0.283	22.197	0.074	76.160
PTQ10 +1% PM6	0.256	24.517	0.093	60.897
PM6 +1% PCE12	0.281	22.358	0.098	57.697

Short discussion:

The changes in the IP properties for PTQ10 when 1% PM6 is added as the secondary donor are relatively small when compared to the changes in PM6 when 1% PCE12 is added. This result is expected since the previously presented miscibility and optical characterizations indicate that PCE12 is highly miscible to PM6 and thereby can form molecular alloys. This is not the case for PTQ10 and PM6, which have been identified to come with much weaker molecular interactions.

Methods

Device fabrication. Solar cells were fabricated in a conventional configuration of ITO/PEDOT:PSS/active layers/PFN-Br/Ag. The ITO substrates were first scrubbed by detergent and then sonicated with deionized water, acetone and isopropanol subsequently, and dried overnight in an oven. The glass substrates were treated by UV-Ozone for 30 min before use. PEDOT:PSS was spin-cast onto the ITO substrates at 7500 rpm for 30 s, and then dried in ambient atmosphere. The blend solution was spin-cast at 2000-2500 rpm for 30 s onto PEDOT:PSS film, followed by a temperature annealing of 100°C for 1 min. A thin PFN-Br layer was coated on the active layer at 3000 rpm, followed by the deposition of Ag (evaporated under < 10-5 Pa through a shadow mask). The optimal active layer thickness is estimated to be about 100-110 nm.

Solar simulation. The current density-voltage (J-V) curves of devices were measured using a Keithley 2400 Source Meter in glovebox under AM 1.5G (100 mW cm-2) using an SAN-EI ELECTRIC solar simulator. The device contact and illuminated area were 0.06 cm^2. A step voltage of 0.1 – 0.5 V with about 5 ms delay time are used.

Absorption and photoluminescence spectroscopy. The steady-state absorption measurements were conducted using UV-Vis-NIR spectrophotometer Lambda 950 from Perkin Elmer while PL spectra were collected using InVia (Renishaw) spectrometer with sample excitation at 632.8 nm laser.

Sensitively measured external quantum efficiency. The sEQE spectra of devices were collected at short-circuit conditions using monochromatic illumination from a combination of a monochromator and 150 W tungsten lamp. An optical chopper modulated the light beam with a frequency of 405 Hz, and the device photocurrent was measured as a function of the incident photon energy (wavelength) using a lock-in amplifier (Stanford Instrument SR 850), and the incident light power was measured with a power meter (Newport 918D-UV-0D3R).

Grazing incidence small-angle X-ray scattering (GISAXS). GIWAXS/GISAXS measurements were performed on a XEUSS SAXS/WAXS system (XENOCS, France), Hong Kong University of Science and Technology (Guang Zhou), (HKUST (GZ), Guangzhou). The films were fabricated following the conditions of the best devices.

Time-Resolved Spectroscopy (TAS). Femtosecond transient absorption measurements were performed using a commercial pump–probe spectrometer (Helios, Ultrafast Systems) at King Abdullah University of Science and Technology (KAUST). The output of a Ti:sapphire regenerative amplifier (Astrella, Coherent; 800 nm center wavelength, ~150 fs pulse duration, 1 kHz repetition rate) was split to generate pump and probe pulses. Pump pulses at 800 nm were produced using a spectrally tunable optical parametric amplifier (TOPAS). The output was further spectrally cleaned using a bandpass filter (800 ± 10 nm; Newport) to suppress residual wavelengths and improve pump spectral purity. The pump fluence was kept constant at 3 μJ cm^{-2}, and the pump beam was focused to a spot diameter of ~0.03 cm at the sample. A broadband white-light continuum probe was generated by focusing a fraction of the 800 nm beam into a 2-mm CaF_2 crystal. The temporal delay between pump and probe pulses was controlled using a computer-controlled motorized delay stage in the probe beam path. The white-light probe was split into signal and reference beams to reduce pulse-to-pulse fluctuations and improve the signal-to-noise ratio. The pump beam was modulated using a synchronized mechanical chopper operating at 500 Hz, blocking every other pump pulse, and the pump and probe beams were spatially overlapped at the sample. The absorption change (ΔA) was measured based on the time delay and wavelength (λ). The IRF for the TA was measured to be 168 fs. For fluence-dependent TAS, a similar Helios-based TA setup was used at the photophysics laboratory of Prof. Sum Tze Chien at Nanyang Technological University (NTU).

Neutron reflectometry (NR). The NR measurements were carried out on the Spatz time-of-flight neutron reflectometer at the OPAL reactor, Australian Nuclear Science and Technology Organisation (ANSTO).[5] The wavelength resolution was set to ~5% ($\Delta\lambda/\lambda$) by operating choppers 1 and 2 as a pair at 25 Hz. Reflectivity data were acquired using two incident angles, 0.70° (3600 s) and 3.50° (9000 s), providing a combined momentum transfer range of $0.008 \leq q \leq 0.26$ $Å^{-1}$. The momentum transfer is defined as $q = 4\pi \sin(\theta)/\lambda$, where θ is the incident angle and λ is the neutron wavelength. The illuminated footprint on the sample was 13 mm × 12 mm. The data were reduced using a Jupyter notebook workflow with the *refnx* package.[6] The reduction included detector efficiency correction, conversion from time-of-flight to wavelength, calculation and re-binning the data to the instrument resolution, and stitching the two angle datasets within the overlap region to obtain a continuous reflectivity profile. The reflectivity was then normalized by scaling the critical edge to unity. Model fitting was performed in *refnx* using a slab

representation,[6] in which each layer is parameterized by its thickness, interfacial roughness, and scattering length density (SLD). The SLD is defined as SLD = $\sum b_i/V_m$, where b_i is the scattering length of the atoms in the system, and V_m is the molecular volume. Parameters were refined by minimizing the mismatch between the measured and calculated reflectivity using a differential evolution algorithm.

References

1. Wong, J., S.T. Omelchenko, and H.A. Atwater, *Impact of Semiconductor Band Tails and Band Filling on Photovoltaic Efficiency Limits.* ACS Energy Letters, 2021. **6**(1): p. 52-57.
2. Zhang, Y. and G. Li, *Functional Third Components in Nonfullerene Acceptor-Based Ternary Organic Solar Cells.* Accounts of Materials Research, 2020. **1**(2): p. 158-171.
3. Tamai, Y., et al., *Ultrafast Long-Range Charge Separation in Nonfullerene Organic Solar Cells.* ACS Nano, 2017. **11**(12): p. 12473-12481.
4. Li, Z., et al., *Ultrafast charge transfer and suppressed non-radiative energy loss enabled by trifluoromethyl-substituted low-cost polymer donors for efficient organic solar cells.* Science China Chemistry, 2025. **68**(8): p. 3797-3806.
5. Le Brun, A.P., et al., *Spatz: The Time-Of-Flight Neutron Reflectometer with Vertical Sample Geometry at the OPAL Research Reactor.* Journal of Applied Crystallography, 2023. **56**(1): p. 18-25.
6. Nelson, A.R.J. and S.W. Prescott, *Refnx: Neutron and X-Ray Reflectometry Analysis in Python.* Journal of Applied Crystallography, 2019. **52**(1): p. 193-200.